Role of a Pacific Easterly Wave in the Genesis of Hagupit (2008)

CHEN ZHAO,[a] TIM LI,[b,c,d] AND MINGYU BI[b]

[a] *Institute of Natural Resources and Environmental Audits, School of Government Audit, Nanjing Audit University, Nanjing, China*
[b] *Key Laboratory of Meteorological Disaster, Ministry of Education/Joint International Research Laboratory of Climate and Environmental Change/Collaborative Innovation Center on Forecast and Evaluation of Meteorological Disasters, Nanjing University of Information Science and Technology, Nanjing, China*
[c] *International Pacific Research Center, School of Ocean and Earth Science and Technology, University of Hawai'i at Mānoa, Honolulu, Hawaii*
[d] *Department of Atmospheric Sciences, School of Ocean and Earth Science and Technology, University of Hawai'i at Mānoa, Honolulu, Hawaii*

(Manuscript received 27 June 2021, in final form 1 September 2022)

ABSTRACT: The Advanced version of the Weather Research and Forecasting (WRF-ARW) Model is used to investigate the influence of an easterly wave (EW) on the genesis of Typhoon Hagupit (2008) in the western North Pacific. Observational analysis indicates that the precursor disturbance of Typhoon Hagupit (2008) is an easterly wave (EW) in the western North Pacific, which can be detected at least 7 days prior to the typhoon genesis. In the control experiment, the genesis of the typhoon is well captured. A sensitivity experiment is conducted by filtering out the synoptic-scale (3–8-day) signals associated with the EW. The absence of the EW eliminates the typhoon genesis. Two mechanisms are proposed regarding the effect of the EW on the genesis of Hagupit. First, the background cyclonic vorticity of the EW could induce the small-scale cyclonic vorticities to merge and develop into a system-scale vortex. Second, the EW provides a favorable environment in situ for the rapid development of the typhoon disturbance through a positive moisture–convection feedback.

KEYWORDS: North Pacific Ocean; Cyclogenesis/cyclolysis; Mesoscale processes

1. Introduction

Tropical cyclone (TC) genesis involves interactions among multiscale motions (Ritchie and Holland 1997; Li 2012; Cao et al. 2018). Apart from the favorable large-scale environmental conditions that were summarized by Gray (1968), Ritchie and Holland (1999) indicated that there were three types of environmental flow regimes associated with TC genesis in the western North Pacific (WNP): monsoon gyre, the monsoon shear line, and the monsoon confluence zone. While these large-scale dynamic and thermodynamic conditions play vital roles in providing a background condition for tropical storm development, the exact timing of TC formation depends critically on precursory synoptic-scale disturbances (Li et al. 2003; Fu et al. 2007). Previous studies have identified several precursor disturbances associated with TC genesis in the WNP, including northwest–southeast-oriented synoptic wave trains (SWT) (Lau and Lau 1990; Chang et al. 1996; Li 2006; Xu et al. 2014), Rossby wave energy dispersion from a preexisting TC (TCED) (Frank 1982; Briegel and Frank 1997; Ritchie and Holland 1997; Li et al. 2003; Li and Fu 2006; Li et al. 2006; Ge et al. 2010), mixed Rossby–gravity waves (Frank and Roundy 2006) and Pacific easterly waves (EWs) (Ritchie and Holland 1999; Fu et al. 2007; Chen et al. 2008).

The effect of the EWs on TC genesis in the tropical Atlantic was discovered by Riehl (1948). He demonstrated that a low-level cyclone within a wave collocated with an upper level ridge favored TC genesis. Later, EWs and their potential role in TC genesis in the WNP were detected (e.g., Yanai et al. 1968; Chang 1970; Reed and Recker 1971). Different from the Atlantic EW, the origin of the Pacific EW arose from the southward energy propagation of Rossby waves from the upper-tropospheric jet in the North Pacific (Tam and Li 2006). The role of EW forcing under an idealized confluent mean flow in TC genesis was investigated by Kuo et al. (2001). They demonstrated in a barotropic model that the scale contraction of easterly waves could lead to the accumulation of kinetic energy in a critical longitude where the westerly monsoon winds meet the easterly trade winds. This energy accumulation mechanism may lead to the successive development of a TC cluster at the critical longitude. With the use of QuikSCAT data, Fu et al. (2007) found that 21% of cyclogenesis events in the WNP were associated with EWs during the summers of 2000 and 2001. Chen et al. (2008) showed that 80% of TC genesis in the WNP was influenced by EWs directly or indirectly.

A "marsupial theory" was developed to describe the transformation from a synoptic-scale EW to a tropical depression (Dunkerton et al. 2009; Montgomery et al. 2010; Wang et al. 2010a,b; Fang and Zhang 2011; Rajasree et al. 2016a,b). The Kelvin cat's-eye within a critical layer (defined as the location where mean flow minus the wave speed equals zero) of an EW was shown to be critical for TC formation. The cat's-eye is located over the intersection of the wave trough axis and the critical layer, acting like a "pouch" to protect an initial weak vortex from hostile environment until it is strengthened into a self-sustained entity.

TC genesis may be divided into two stages. The first stage involves a transition from randomly generated small-scale vortical hot towers (VHTs) to an organized mesoscale vortex

Corresponding author: Tim Li, timli@hawaii.edu

DOI: 10.1175/WAF-D-21-0105.1

(Li et al. 2006; Li 2012). The second stage is characterized by a rapid deepening of the moist column within the vortex core and a buildup of an upper-level warm core (Ge et al. 2013). Typically, a precursory synoptic-scale disturbance occurs in the lower troposphere. TC genesis associated with the low-level disturbance is sometimes called a "bottom-up" process. In contrast, a "top-down" process suggests that low-level winds are strengthened due to a midlevel vortex (e.g., Bister and Emanuel 1997; Ritchie and Holland 1997; Nolan et al. 2007). A midlevel vortex may occur in a stratiform cloud region, due to raindrop-induced evaporative cooling. This midlevel vortex may cause subsequent TC formation (Li 2012). Given the same vertically integrated vorticity strength, the low-level vortex appears more efficient than the midlevel vortex in TC genesis (Li 2012).

The objective of the current study is to reveal observed characteristics of precursory EW signals prior to the genesis of Typhoon Hagupit (2008) and role of EW on TC genesis. The data and model experiment design are introduced in section 2. Section 3 describes the large-scale environment and EW characteristics. The role of the EW in the TC formation and associated atmospheric processes are investigated in section 4 through high-resolution numerical model simulations. Finally, conclusions and discussions are given in the last section.

2. Data and model experiment design

a. Data

The data used in this study are 6-hourly National Centers for Environmental Prediction (NCEP) Final Operational Global Analysis (FNL), Joint Typhoon Warning Center (JTWC) best track data, and Multi-Functional Transport Satellite (MTSAT) infrared (IR) satellite data (http://weather.is.kochi-u.ac.jp/sat/ALL/) with a spatial resolution of 0.5° × 0.5° and temporal resolution one hour. The FNL includes three-dimensional atmospheric variables such as wind, temperature, geopotential height, and moisture fields at standard constant pressure levels. Its horizontal resolution is 0.5° × 0.5°. The IR data measure the temperature at top of clouds and are used to represent the strength of convective activity.

b. Model and experiment design

The Advanced Research version of the WRF (ARW) Model, version 3.7 (Skamarock et al. 2008), is used for the simulation of Typhoon Hagupit. The model has triple nested meshes. The outermost domain has a 27-km resolution with 250 × 160 grids. Two inner meshes have the following resolution and grids: 9 km and 511 × 280, and 3 km and 1021 × 601, respectively. The innermost domain moves automatically following the simulated TC. The model has 45 vertical layers with the model top at 10 hPa. The single-moment six-class microphysics scheme (WSM6) (Hong et al. 2006) is used in all meshes and the Betts–Miller–Janjić convective scheme is applied to the two outermost meshes (Janjić 1994, 2000). Other physics parameterizations used include a Dudhia shortwave radiation scheme (Dudhia 1989), a Rapid Radiative Transfer Model (RRTM) longwave radiation scheme (Mlawer et al. 1997) and the Yonsei University boundary layer scheme (Noh et al. 2003). The initial conditions and the outermost domain lateral boundary forcing are derived from NCEP-FNL 6-hourly analyses with 1.0° resolution.

In the control experiment (CTL), the model initial condition is specified from NCEP-FNL at 1200 UTC 16 September 2008, nearly three days prior to declaration of tropical storm status by JTWC. The model was integrated for 90 h. In CTL, the EW perturbation and the mean environmental flow are specified at the initial condition. The method for identifying EW disturbances as TC precursors follows Fu et al. (2007). A Lanczos bandpass filter is performed to extract the 3–8-day signals (Duchon 1979).

To further illustrate the role of EWs on the genesis of Hagupit, a sensitivity experiment (EXP_EW) is conducted, in which the EW perturbation is removed from the initial and lateral boundary conditions. More specifically, the 3–8-day components of the dynamic variables (zonal wind, meridional wind) and thermodynamic variables (air temperature, specific humidity, geopotential height and surface pressure fields) are removed from the total fields. In the experiments, it is necessary to ensure that the time filtering is able to preserve a consistent set of dynamic and thermodynamic fields for selected waves. This is achieved by comparing the filtered wind fields with those calculated from the filtered geopotential height based on the geostrophic balance equation. The difference is very small, indicating that the time filtering basically maintains a balanced relationship.

3. Large-scale environmental flow and EW characteristics

Hagupit (2008) developed from an EW in the western North Pacific. Hagupit was declared as a tropical depression by the JTWC at 1800 UTC 18 September 2008. Just 12 h later, at 0600 UTC 19 September 2008, Tropical Cyclone Hagupit formed with maximum sustained surface wind of 35 kt (1 kt ≈ 0.51 m s^{-1}). Hagupit continued to intensify and was upgraded to a severe typhoon with maximum sustained wind speed 125 kt in the South China Sea. A rough estimate of damage due to Hagupit was the death of more than 67 people and an economic loss of $1 billion (U.S. dollars) (Bell and Montgomery 2010).

The precursory disturbance can be well detected from the total flow field at 850 hPa from the FNL analyses (Fig. 1). The wavelike perturbation can be traced at least 7 days prior to the formation of Tropical Storm Hagupit. Using a high-resolution Year of Tropical Convection (YOTC) dataset, Xu et al. (2013) classified precursory synoptic-scale disturbances for TCs in the WNP during 2008–09 summers and found that the precursor disturbance of Hagupit was an easterly wave. A wavelike pattern with a trough around 160°E is clearly seen from 1200 UTC 12 September onward. Accompanied with the trough was convective activity represented by the IR brightness temperature in the northeast portion of the trough (Fig. 1a). Later, the wave continued propagating westward as it developed. It became a closed cyclonic circulation around

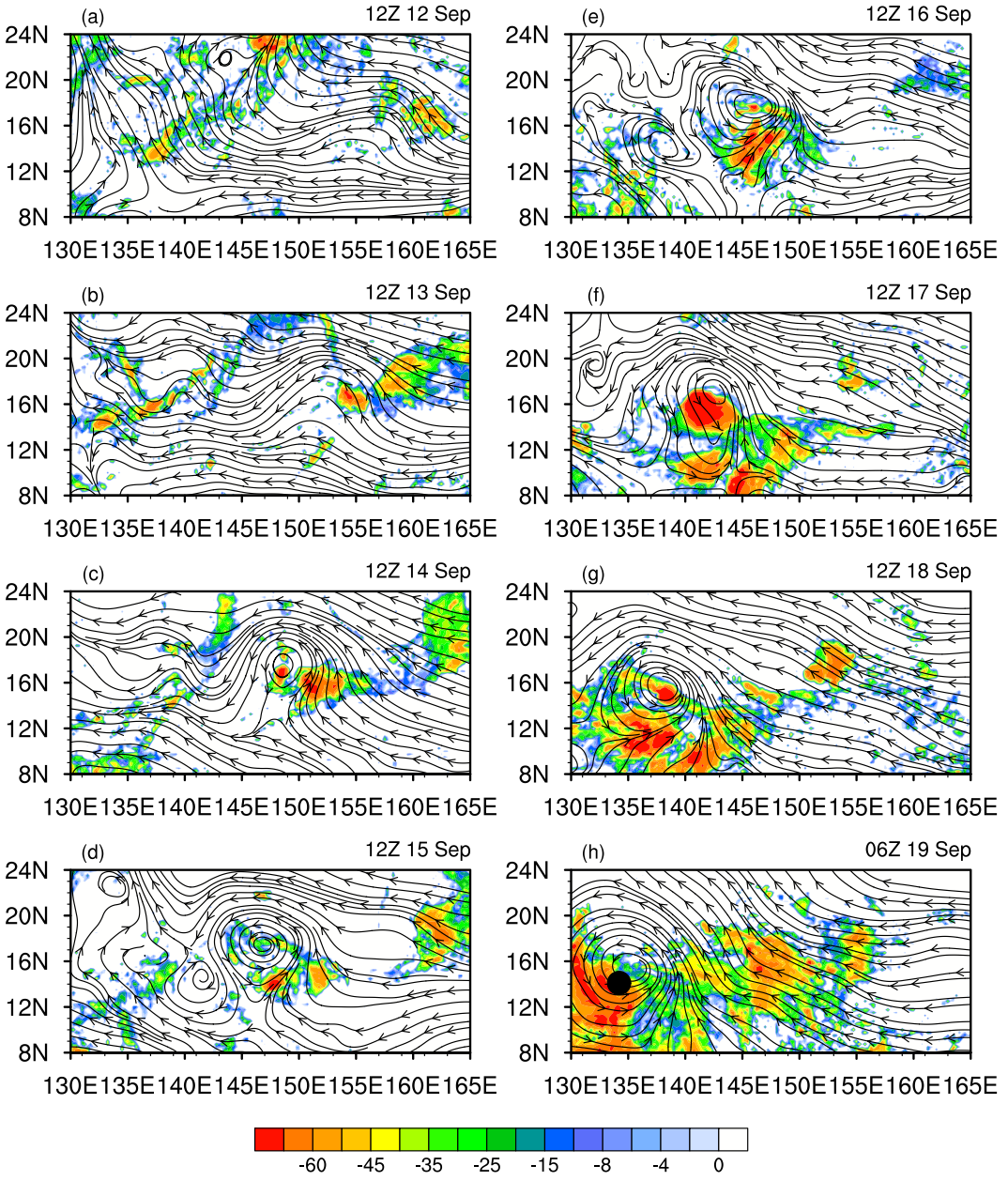

FIG. 1. (a)–(h) Streamlines at 850 hPa from GFS FNL analyses and IR brightness temperature from MTSAT (shading; K) from 1200 UTC 12 Sep to 0600 UTC 19 Sep. The black dot in (h) indicates the tropical storm genesis location on that day.

1200 UTC 14 September. Correspondingly, convective activity also strengthened gradually and shifted to the west of the trough as it entered into an environmental easterly shear region.

Figure 2 illustrates more clearly the easterly wave propagation characteristic. It shows the Hovmöller diagram of 3–8-day filtered meridional wind at 850 hPa averaged over 14°–19°N from 1200 UTC 12 September to 0600 UTC 19 September. There is clear westward propagation in the synoptic-scale meridional wind. The average westward phase speed is about 4.2 m s^{-1}. Additional tests with a narrower latitudinal band (15°–18°N) or a shifted latitudinal band (12°–16°N) resulted in similar phase speeds; thus, phase speed is not sensitive to the choice of the latitudinal range.

To view more clearly the pouch effect, we plotted a similar figure to Fig. 1 but within the Lagrangian framework, where the estimated EW phase speed is removed from the original flow field as an observer who moves zonally at the same speed of the wave. The Lagrangian closed circulation colloquially called the "wave pouch" can protect the EW from dry air

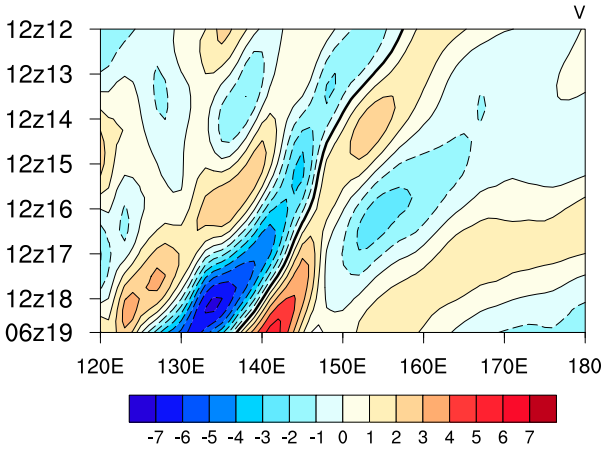

FIG. 2. Hovmöller diagram of the 3–8-day-filtered meridional wind at 850 hPa averaged along 14°–19°N. The thick dashed line indicates the propagation of the EW disturbance.

intrusion and sustain deep convection (Dunkerton et al. 2009; Bell and Montgomery 2010). The relative streamline field is superimposed on the environmental vertical wind shear. (i.e., the difference between the 200- and 850-hPa zonal wind). The shading represents the vertical wind shear. The red line represents the critical latitude or surface, where zonal velocity is equal to the zonal wave phase speed. The critical layer is a layer of finite width due to the nonlinear interaction of the wave with its own critical surface (e.g., Dunkerton et al. 2009; Wang et al. 2010a,b). The black line represents the wave trough axis, which is defined as the region where the meridional velocity vanishes and the maximum relative vorticity appears. The intersection of the critical latitude and the wave trough axis in the lower troposphere pinpoints the cat's-eye or the center of the wave pouch location. In contrast to a wavelike flow in Figs. 1a and 1b, a closed cyclonic circulation with a cat's-eye appears in the wave disturbance (Figs. 3a,b). The vertical wind shear in the pouch region is relatively weak (less than 10 m s^{-1}), which is favorable for TC genesis (Bracken and Bosart 2000). It is worth mentioning that the vertical shear transformed from a westerly shear (Figs. 3a–f) to an easterly shear (Figs. 3g,h) environment as the wave moved westward.

Figure 4 displays the structure and evolution of the EW during the TC genesis period. Different from a typical northwest–southeast-oriented structure of synoptic-scale wave train, the EW with an alternating anticyclonic and cyclonic circulation shows a slightly northeast–southwest distribution (Figs. 4a,c,e,g). A clear cyclonic circulation in low troposphere collocated with an anticyclonic circulation at the upper level and the cyclonic vorticity is mainly confined to the middle and lower troposphere. This vertical structure is in agreement with that of a classic EW (e.g., Reed and Recker 1971; Ritchie and Holland 1999; Chen et al. 2008). Meanwhile, the positive relative vorticity is accompanied with positive relative humidity anomaly (Fig. 4b). Physically, a low-level cyclonic circulation may induce anomalous ascending motion through Ekman pumping process, which can further increase local moisture content through vertical advection. The enhanced moisture content subsequently feeds back to the low-level circulation via enhanced diabatic heating. As the wave moves westward, the cyclonic circulation gradually strengthens and penetrates vertically upward to about 100 hPa. The relative humidity presents positive anomalies in planetary boundary layer (PBL) (Figs. 4d,f,h). The deep-layer vorticity of the EW, along with the positive moisture anomalies in PBL, may contribute greatly to the continuous development of the vortex.

4. Processes associated with Hagupit formation derived from WRF simulations

The observational analysis above indicates the EW with a pouch, which could provide a favorable environmental condition for vortex development (e.g., Dunkerton et al. 2009; Bell and Montgomery 2010). To reveal the influence of the EW on Hagupit formation, we conducted high-resolution WRF simulations. Figure 5 displays the 850-hPa circulations at the model initial time for CTL and EXP_EW. The pattern in EXP_EW is very similar to that in CTL. However, because of the absence of EW, the amplitude of the circulations in EXP_EW is greatly reduced compared with CTL. By comparing the CTL and EXP_EW experiments, one may reveal how the EW influences the TC genesis.

In comparison to the JTWC best track, the CTL reproduces well the observed TC track and the intensity (Figs. 6a,b). Figure 6a shows that the simulated track is close to the observed one during the 90-h integration, especially the westward track, although the simulated genesis location (red typhoon mark) is a little south to the real genesis location (black typhoon mark). In terms of the intensity, the TC intensities are similar for both CTL and the observation. The model reproduces the observed deepening of the minimum sea level pressure around 1200 UTC 18 September when the EW approaches the monsoon trough region. However, when the EW is removed in EXP_EW, the vortex fails to grow throughout the 90-h integration period (Fig. 6b). This indicates the important role of the EW in affecting subsequent TC development. It is noteworthy that the horizontal wind derived from EXP_EW shows that there is still a pouch in the absence of the EW (figure not shown). Therefore, the EW as a pouch has a partial but not decisive effect on tropical cyclone formation.

Given that the model is able to reproduce the realistic evolution of the TC track and intensity, to figure out the physical mechanism of Typhoon Hagupit induced by the EW, a spacial filtering technique following Hendricks et al. (2011) is used to isolate the small-scale (<50 km) and mesoscale (>50 km) motions from the model results. The simulated vorticity fields with small-scale and mesocale are shown in Figs. 7 and 8, respectively. Initially, the small-scale cyclonic vorticity anomalies which may be the cumulus-scale convective clouds or VHTs are randomly distributed around the background cyclonic vorticity (Figs. 7a,e). As the vortex develops, the randomly generated cyclonic vorticity anomalies merge and form a mesoscale core vortex that gradually move toward the center of the background cyclonic vorticity in CTL (Figs. 8a–d).

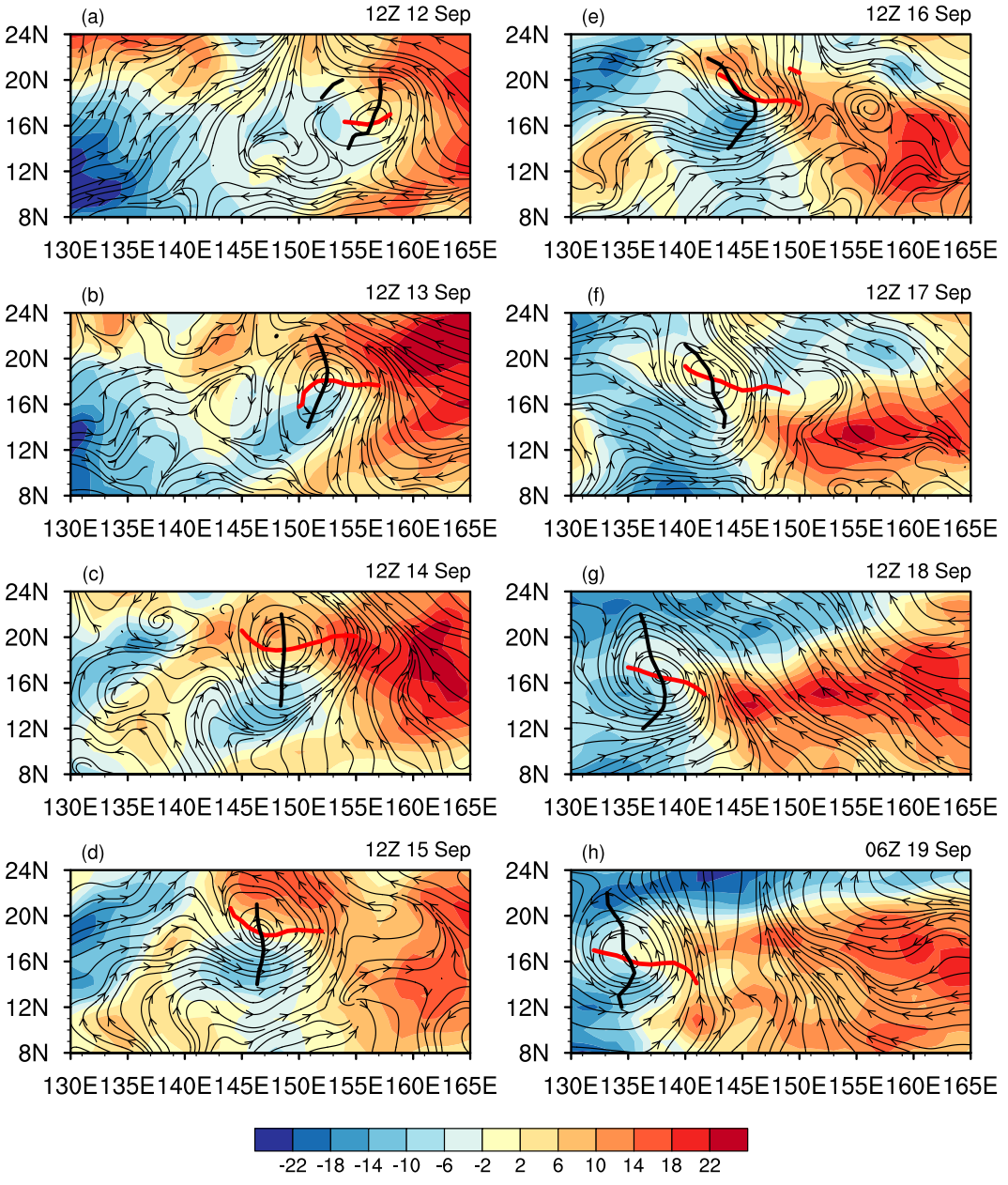

FIG. 3. Streamlines at 850 hPa and vertical wind shear between 200 and 850 hPa (shading; m s^{-1}) from GFS FNL analyses in the Lagrangian framework with the EW from 1200 UTC 12 Sep to 0600 UTC 19 Sep. The black line represents the wave trough axis (where the meridional velocity is zero), and the red line indicates the critical layer latitude (where the zonal flow is equal to the wave phase speed).

Such an aggregation may be caused by the vorticity segregation process (Schecter and Dubin 1999) or closely related to the developing secondary circulation with radial inflow at lower levels (Kilroy et al. 2017a,b). By comparing the CTL and EXP_EW, it shows that the small-scale vorticity features appear during the early stage in EXP_EW but they are much weaker than those in CTL owing to the lack of the EW organization (Figs. 7e–h). Mesoscale vorticity features also develop in earlier stage in EXP_EW (Figs. 8e,f); however, they never develop into a strong mesoscale core vortex due to the less favorable environment in EXP_EW. This confirms that the EW plays an important role in maintaining the continuous development of vortex.

Figure 9 shows the time–vertical cross section of divergence, relative humidity, relative vorticity, tangential wind, vertical velocity, and temperature fields averaged within a radius of 200 km from the pouch center in CTL. These fields are derived from the innermost mesh with a 3-km horizontal

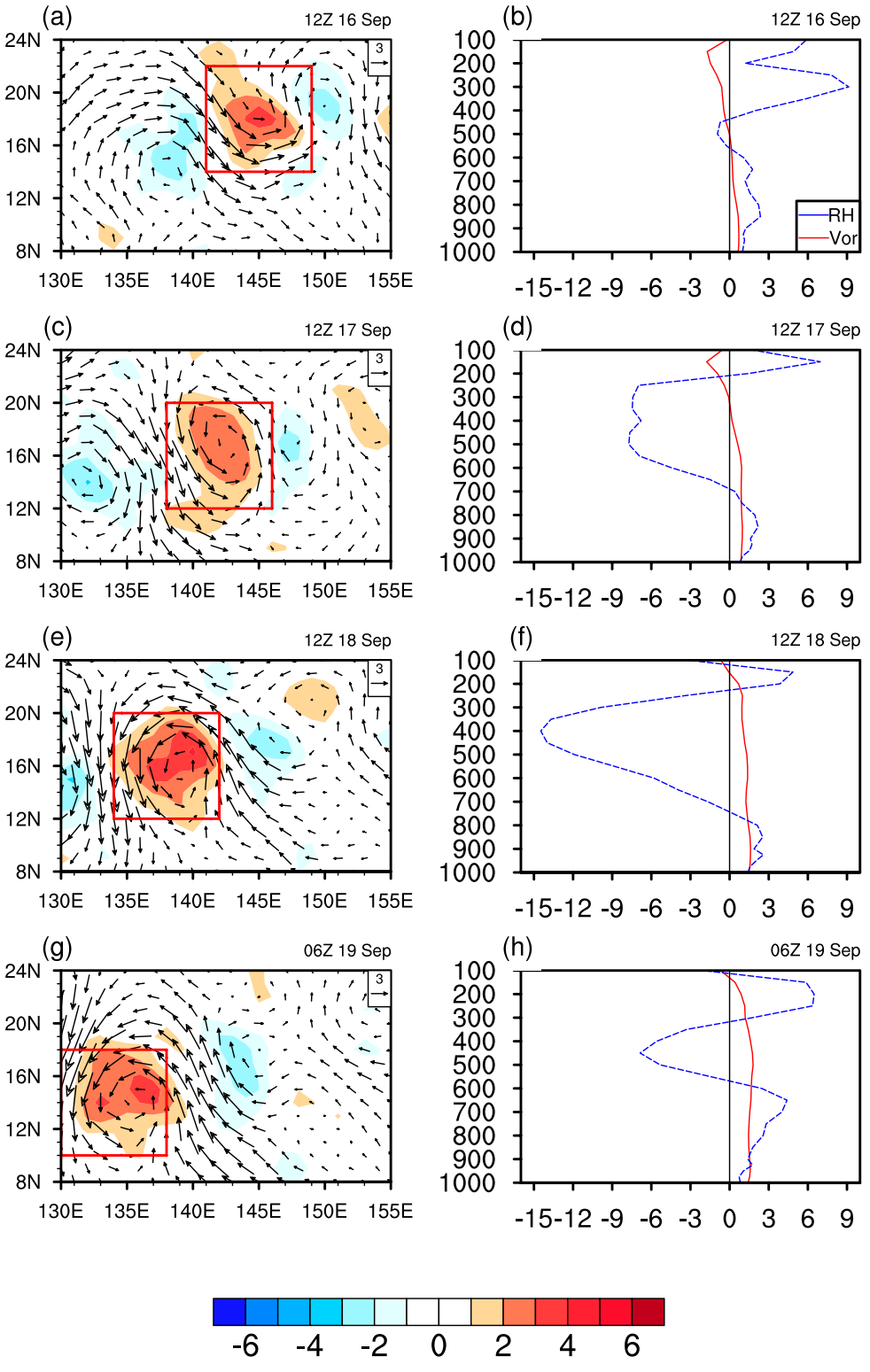

FIG. 4. (left) Horizontal wind (vector; m s^{-1}) and relative vorticity (shading; 10^{-5} s^{-1}) at 850 hPa, and (right) vertical profiles of area-averaged (8° × 8°) relative vorticity (red line; 10^{-5} s^{-1}) and relative humidity (blue line; %) from 3- to 8-day-filtering fields at (a),(b) 1200 UTC 16 Sep; (c),(d) 1200 UTC 17 Sep; (e),(f) 1200 UTC 18 Sep; (g),(h) 0600 UTC 19 Sep. The red box represents the major circulation region. The black line indicates the zero value of each parameter.

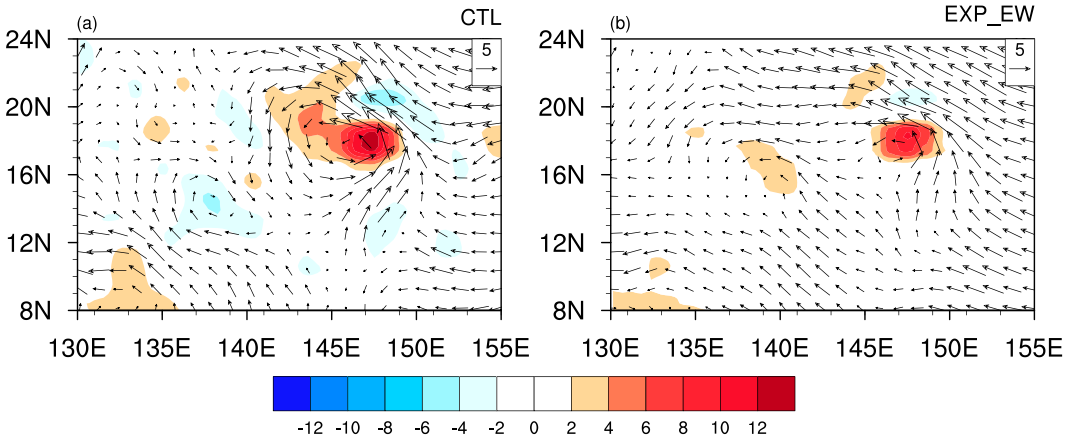

FIG. 5. Wind (vector; m s^{-1}) and relative vorticity (shading; 10^{-5} s^{-1}) at 850 hPa at the model initial time in (a) the control experiment CTL and (b) sensitivity experiment EXP_EW.

resolution and a 3-h time interval. It is interesting to note that the maximum vorticity appears in PBL. Different from the top-down scenario, which assumes that the generation of low-level vorticity by some form of vorticity transport or projection downward from the midlevels, the current TC development is characterized by a bottom-up process, that is, the vorticity maximum is located at the low level initially and then gradually extends to middle and upper troposphere. In addition, during the initial development, the PBL vorticity exhibits a clear oscillatory growth. For instance, the vorticity grows rapidly between 1200 UTC 17 September and 0000 UTC 18 September, slows down or even decays afterward, and re-intensifies around 1200 UTC 18 September (Fig. 9b). Such an oscillation is consistent with the divergence and vertical velocity oscillation shown in Figs. 9a and 9c, and was attributed to the transition from a convective regime to a stratiform regime as shown in Li et al. (2006). The convergence (divergence) in PBL is well collocated with cyclonic (anticyclonic) vorticity. The ascending motion leads to PBL convergence and the downdraft leads to PBL divergence (Fig. 9a). The vertical motion also regulates the moisture via vertical moisture transport, resulting in the alternative change of relative humidity in the midtroposphere (Fig. 9b). It is worth noting that a remarkable deep updraft emerges at around 1200 UTC 18 September, just 18 h prior to the genesis of Hagupit. The maximum tangential wind shows a rapid increase after the bursts of intense deep convection. Meanwhile a warming core begins to form at the height of 12–14 km at the same time (Fig. 9d). How does this upper-tropospheric warming occur? For a mature TC, an upper-level warm core could result from adiabatic subsidence (Chen and Zhang 2013) or eddy radial advection of potential temperature (Stern and Zhang 2013) within the eye of a TC. However, at 1200 UTC 18 September, the TC has not formed yet, and the vortex is characterized by an embedded meso-γ-scale structure beneath strong upward motions aloft. Most of these deep and intense systems are meso-γ-scale convective bursts (CBs). CBs are traditionally defined as intense meso-γ-scale convective cells with updraft maximized in the upper troposphere. Following the definition used by Cecelski and Zhang (2013), we designate a convective cell as a CB when it is characterized by an updraft greater than 8 m s^{-1} above 600 hPa.

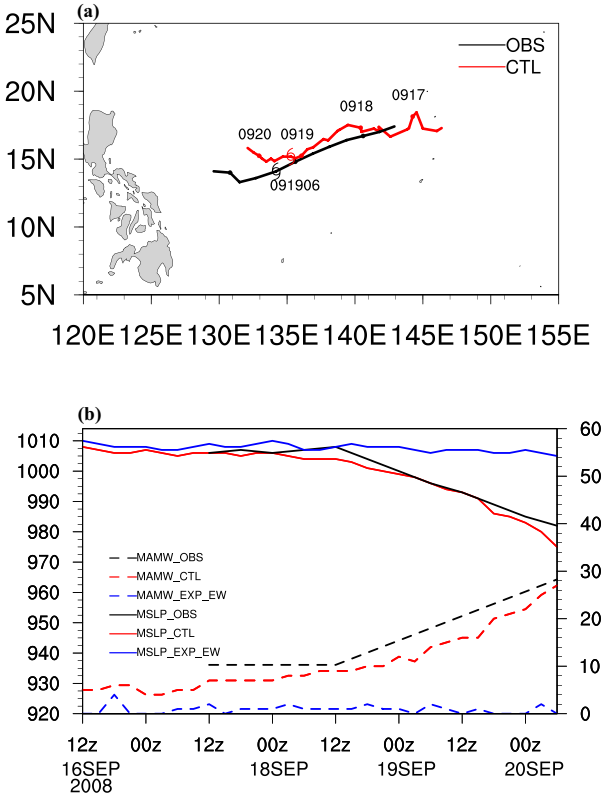

FIG. 6. (a) Observed Hagupit track (black) and simulated track in CTL (red) with black and red typhoon marks denoting the observed and simulated genesis locations; (b) time series of the observed and simulated minimum sea level pressure (solid; hPa) and maximum wind speed at 10 m (dashed; m s^{-1}).

Applying the definition of CBs, it shows clearly that some meso-γ-scale structures are CBs, with the cells characterized

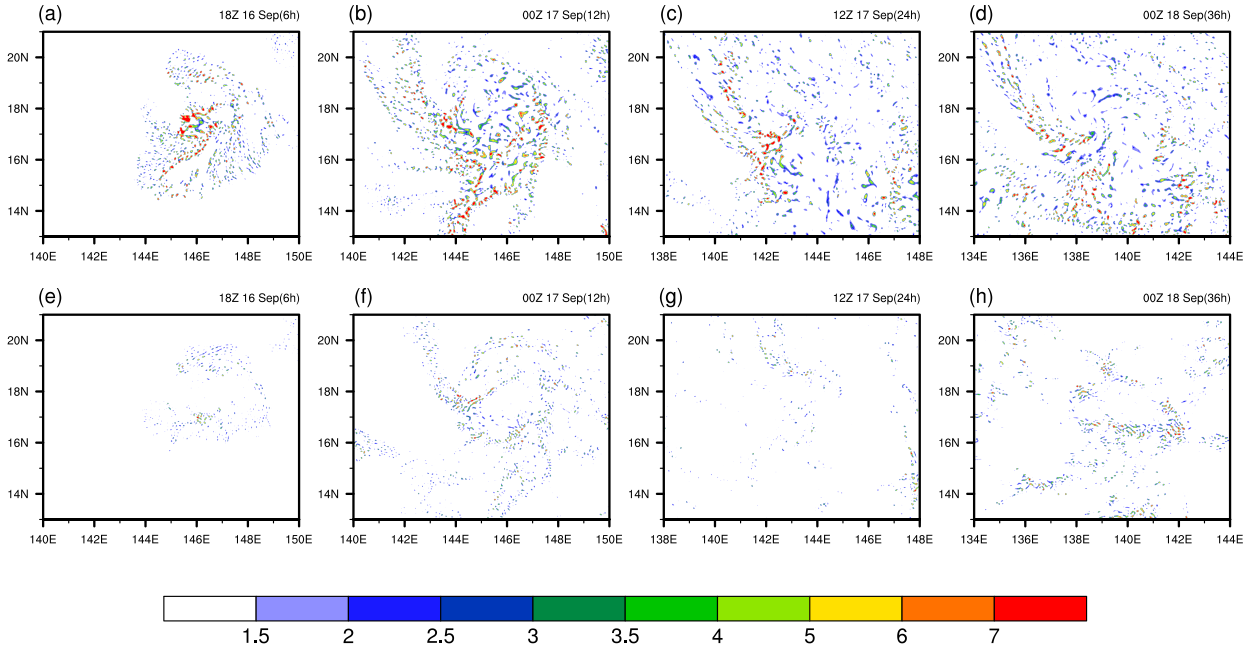

FIG. 7. Relative vorticity (shading; 10^{-5} s^{-1}) with horizontal scale smaller than 50 km at 850 hPa from 1800 UTC 16 Sep to 0000 UTC 18 Sep in (top) CTL and (bottom) EXP_EW (relative vorticities are from 3-km resolution grid output).

by upward velocities in excess of 8 m s^{-1} in the 250–150-hPa layer. Figure 10a illustrates the horizontal map of the CBs. Collocated with the CBs are warm temperatures and large cloud ice mixing ratios within 250–150-hPa layer (Fig. 10b). A vertical cross section (Fig. 10c) reveals that cloud ice concentrates occur primarily between 400 and 100 hPa. The consistent horizontal and vertical patterns suggest that the upper-tropospheric warming prior to the TC genesis is primarily caused by the CB induced latent heating. Compensating subsidence seems to have little role in causing the upper-

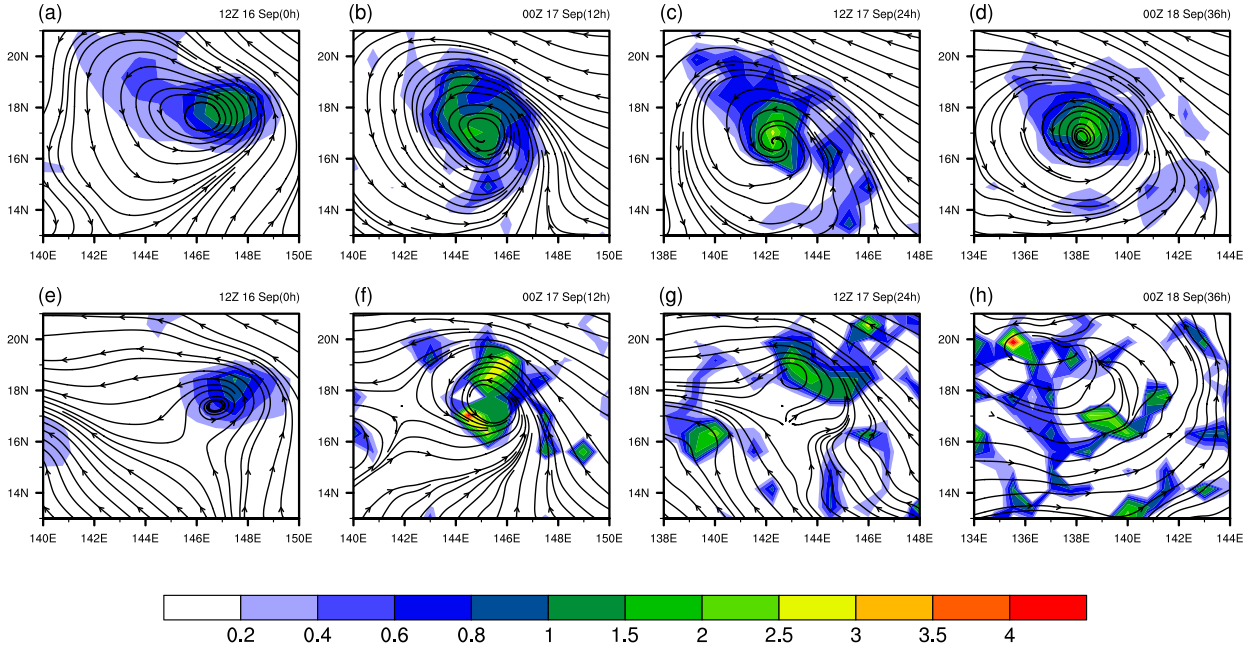

FIG. 8. Streamline and relative vorticity (shading; 10^{-5} s^{-1}) with horizontal scale larger than 50 km at 850 hPa from 1200 UTC 16 Sep to 0000 UTC 18 Sep in (top) CTL and (bottom) EXP_EW (streamline and relative vorticity are from 3-km resolution grid output).

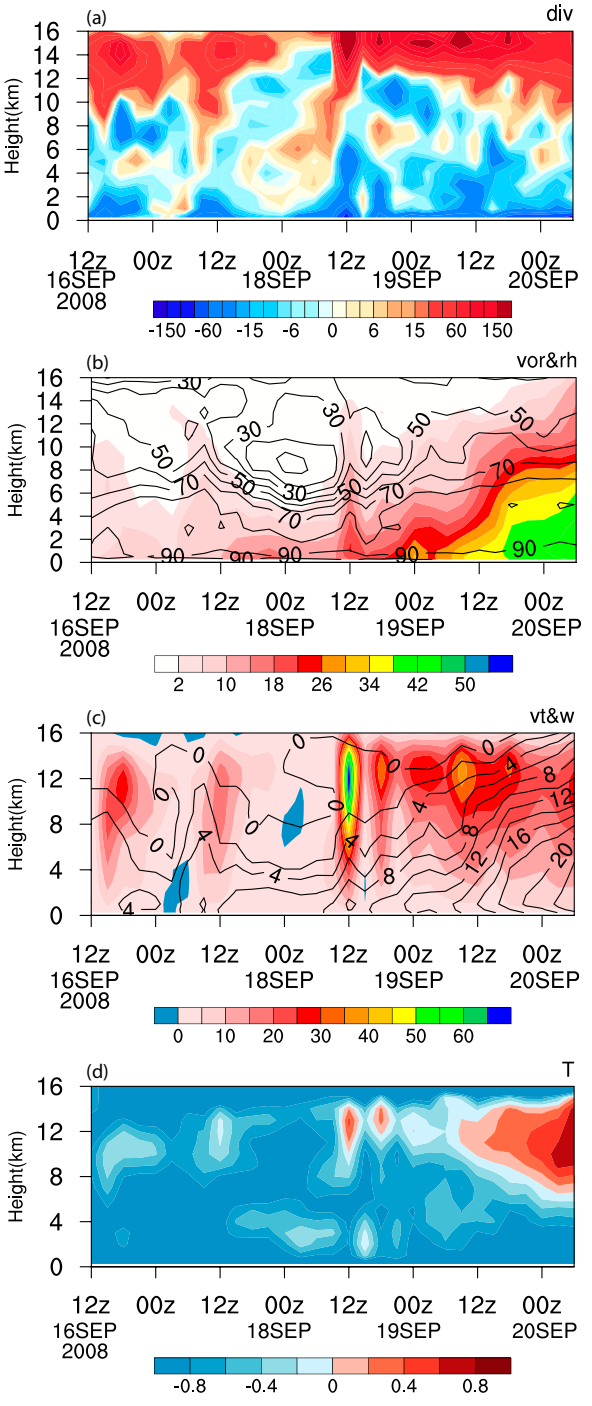

FIG. 9. Time–vertical cross sections of (a) divergence (shading; 10^{-5} s^{-1}), (b) relative humidity (contour; %) and relative vorticity (shading; 10^{-5} s^{-1}), (c) tangential velocity (contour; m s^{-1}) and vertical velocity (shading; cm s^{-1}), and (d) the temperature deviation (K; defined as a difference with the average temperature within a radius of 500 km from the center) fields averaged over a radius of 200 km in the control experiment.

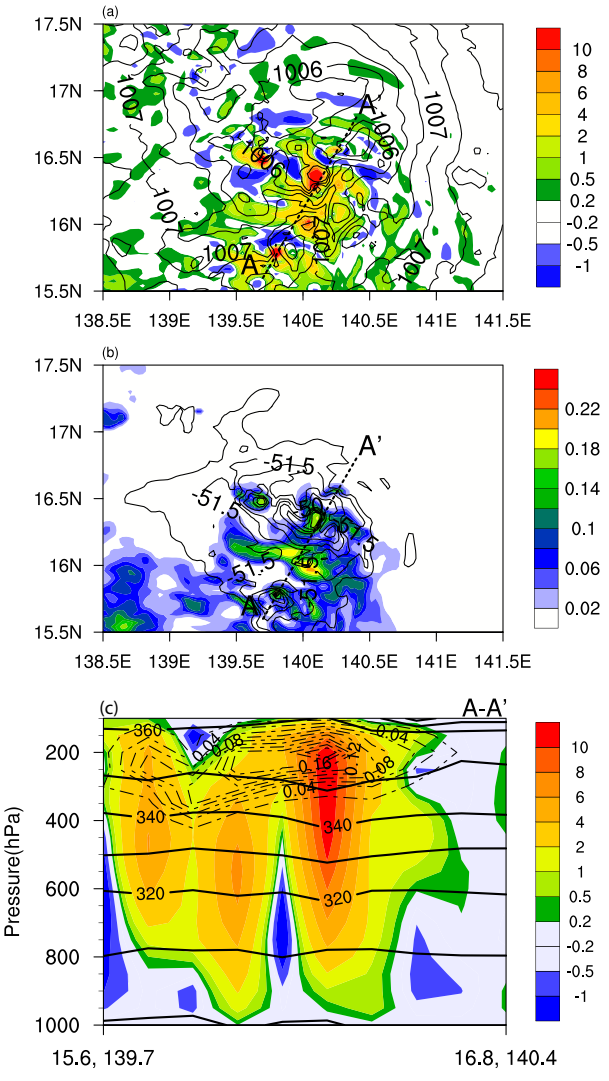

FIG. 10. (a) The horizontal patterns of vertical velocity (shading; m s^{-1}) averaged at 250–150 hPa and the sea level pressure field (contour; hPa), (b) 250–150-hPa-averaged temperature (contour; °C) and cloud ice mixing ratio (shading; g kg^{-1}) fields, and (c) vertical cross section of vertical velocity (shading; m s^{-1}), cloud ice mixing ratio (dashed contours; g kg^{-1}), and potential temperature (solid contours; K) along the dashed line A–A′ shown in (a) and (b) at 1200 UTC 18 Sep.

tropospheric warming [consistent with the Stern and Zhang (2013)].

With the continuous development of the TC, the warm core becomes stronger and stronger, and extends downward to middle troposphere (Fig. 9d). According to the hydrostatic equation, an upper-level warm core is able to cause a greater surface pressure fall than a lower-level warm core (Hirschberg and Fritsch 1993; Holland 1997). Accompanying the warm core is a marked decrease of the minimum sea level pressure (Fig. 6b). This strengthens the boundary layer convergence and updrafts along the eyewall, which further lower the surface pressure through a circulation–convection feedback.

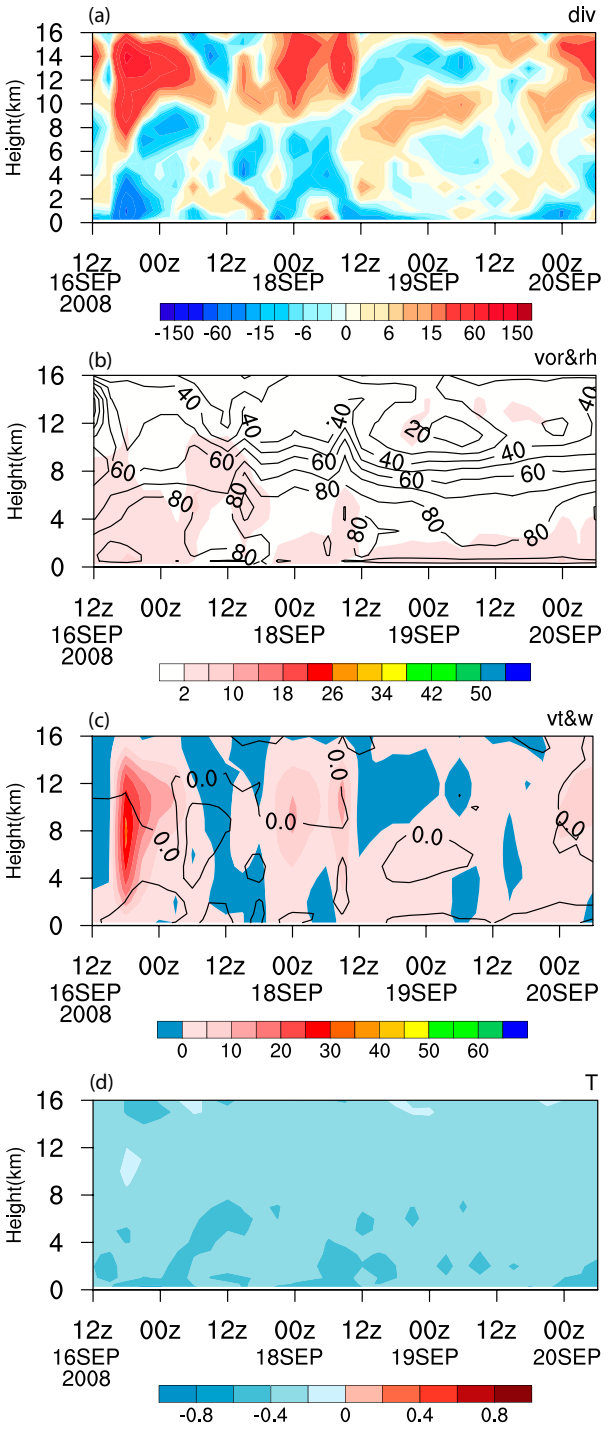

FIG. 11. As in Fig. 7, but for EXP_EW.

Figure 11 displays the time–height section of area-averaged divergence, relative humidity, relative vorticity, tangential wind, vertical velocity, and temperature in EXP_EW. Since there is no TC genesis in EXP_EW, the area average here is simply based on the vortex center location in CTL. Comparing Figs. 9 and 11, one may notice that the vorticity oscillating development feature in both CTL and EXP_EW. A distinct difference lies in that the vorticity penetrate to high altitude in CTL, whereas the vorticity is confined to the PBL in EXP_EW. Relative humidity field shows a similar feature. However, compared to CTL in which the moisture can penetrate into much deep layer, the moisture in EXP_EW is much shallower (Figs. 9b and 11b). A maximum updraft appears in the initial 24 h but the vertical motion diminishes as time goes forward. Considering that the sole difference between CTL and EXP_EW is the presence of the EW, it is conceivable that the cyclonic circulation and moisture related to EW is very important to provide a favorable environment for TC genesis. The removal of the EW in EXP_EW eliminates the reoccurrence of the continuous convective updrafts, which is necessary for the genesis of Hagupit.

5. Conclusions and discussion

The precursory synoptic-scale disturbance for Typhoon Hagupit (2008) is a westward-propagating EW and the wave signal can be traced back at least 7 days prior to the typhoon genesis. Similar to previous studies (Dunkerton et al. 2009; Wang et al. 2010a; Montgomery et al. 2010), the easterly wave contained a pouch that favored the development of a TC-like vortex and protected the disturbance from hostile exterior influence.

The genesis of Typhoon Hagupit is well reproduced using a WRF Model with a high-resolution configuration sufficient to represent mesoscale processes. In the control simulation, the total fields from the FNL data are included. Sensitivity experiment is conducted by removing synoptic-scale signals associated with the EW. The model reproduces well the genesis of Typhoon Hagupit in the presence of the EW in control simulation. For Typhoon Hagupit, removing the EW during the pre-genesis period eliminates the cyclone genesis. Through the diagnosis of the observational analysis and simulated results, two mechanisms are proposed regarding the role of the EW. First, the EW provides a background cyclonic vorticity, which is favorable for the aggregation of mesoscale vertical vorticity and formation of a mesoscale care vortex. The second mechanism is that the EW provides a favorable large-scale environment for the genesis of Hagupit. The EW that displays a cyclonic vorticity in PBL and is collocated with the proper moisture could trigger sustainable ascending motion through Ekman pumping. The upward motion and convective heating further induce low-level convergence, leading the increase of vorticity. This moisture and convective circulation feedback is crucial in leading to the continuous development of vorticities.

Although the current work demonstrates that Typhoon Hagupit genesis is spawned in the pouch of an easterly wave, which influence typhoon genesis through two mechanisms mentioned above, caution needs to be taken in generalizing the finding from this single case study. More case studies are needed to understand the similarity and difference of TC genesis mechanisms among different cyclogenesis events.

Acknowledgments. This work was supported by NSFC Grant 42088101, NSF AGS-2006553, NOAA NA18OAR4310282, and NAU KYPT270492.

Data availability statement. Data related to this paper can be downloaded from the following. JTWC best track data, https://www.metoc.navy.mil/jtwc/jtwc.html?best-tracks; NCEP/FNL data, https://rda.ucar.edu/datasets/ds083.2/; and MTSAT satellite data, http://weather.is.kochi-u.ac.jp/archive-e.html.

REFERENCES

Bell, M. M., and M. T. Montgomery, 2010: Sheared deep vertical convection in pre-depression Hagupit during TCS08. *Geophys. Res. Lett.*, **37**, L06802, https://doi.org/10.1029/2009GL042313.

Bister, M., and K. A. Emanuel, 1997: The genesis of Hurricane Guillermo: TEXMEX analyses and a modeling study. *Mon. Wea. Rev.*, **125**, 2662–2682, https://doi.org/10.1175/1520-0493(1997)125<2662:TGOHGT>2.0.CO;2.

Bracken, W. E., and L. F. Bosart, 2000: The role of synoptic-scale flow during tropical cyclogenesis over the North Atlantic Ocean. *Mon. Wea. Rev.*, **128**, 353–376, https://doi.org/10.1175/1520-0493(2000)128<0353:TROSSF>2.0.CO;2.

Briegel, L. M., and W. M. Frank, 1997: Large-scale influences on tropical cyclogenesis in the western North Pacific. *Mon. Wea. Rev.*, **125**, 1397–1413, https://doi.org/10.1175/1520-0493(1997)125<1397:LSIOTC>2.0.CO;2.

Cao, X., R. Wu, and M. Bi, 2018: Contributions of different time-scale variations to tropical cyclogenesis over the western North Pacific. *J. Climate*, **31**, 3137–3153, https://doi.org/10.1175/JCLI-D-17-0519.1.

Cecelski, S. F., and D.-L. Zhang, 2013: Genesis of Hurricane Julia (2010) within an African easterly wave: Low-level vortices and upper-level warming. *J. Atmos. Sci.*, **70**, 3799–3817, https://doi.org/10.1175/JAS-D-13-043.1.

Chang, C.-P., 1970: Westward propagating cloud patterns in the tropical Pacific as seen from composite satellite photographs. *J. Atmos. Sci.*, **27**, 133–138, https://doi.org/10.1175/1520-0469(1970)027<0133:WPCPIT>2.0.CO;2.

——, J.-M. Chen, P. A. Harr, and L. E. Carr, 1996: Northwestward-propagating wave patterns over the tropical western North Pacific during summer. *Mon. Wea. Rev.*, **124**, 2245–2266, https://doi.org/10.1175/1520-0493(1996)124<2245:NPWPOT>2.0.CO;2.

Chen, H., and D.-L. Zhang, 2013: On the rapid intensification of Hurricane Wilma (2005). Part II: Convective bursts and the upper-level warm core. *J. Atmos. Sci.*, **70**, 146–162, https://doi.org/10.1175/JAS-D-12-062.1.

Chen, T.-C., S.-Y. Wang, M.-C. Yen, and A. J. Clark, 2008: Are tropical cyclones less effectively formed by easterly waves in the western North Pacific than in the North Atlantic? *Mon. Wea. Rev.*, **136**, 4527–4540, https://doi.org/10.1175/2008MWR2149.1.

Duchon, C. E., 1979: Lanczos filtering in one and two dimensions. *J. Appl. Meteor. Climatol.*, **18**, 1016–1022, https://doi.org/10.1175/1520-0450(1979)018<1016:LFIOAT>2.0.CO;2.

Dudhia, J., 1989: Numerical study of convection observed during the Winter Monsoon Experiment using a mesoscale two-dimensional model. *J. Atmos. Sci.*, **46**, 3077–3107, https://doi.org/10.1175/1520-0469(1989)046<3077:NSOCOD>2.0.CO;2.

Dunkerton, T. J., M. T. Montgomery, and Z. Wang, 2009: Tropical cyclogenesis in a tropical wave critical layer: Easterly waves. *Atmos. Chem. Phys.*, **9**, 5587–5646, https://doi.org/10.5194/acp-9-5587-2009.

Fang, J., and F. Zhang, 2011: Evolution of multiscale vortices in the development of Hurricane Dolly (2008). *J. Atmos. Sci.*, **68**, 103–122, https://doi.org/10.1175/2010JAS3522.1.

Frank, W. M., 1982: Large-scale characteristics of tropical cyclones. *Mon. Wea. Rev.*, **110**, 572–586, https://doi.org/10.1175/1520-0493(1982)110<0572:LSCOTC>2.0.CO;2.

——, and P. E. Roundy, 2006: The role of tropical waves in tropical cyclogenesis. *Mon. Wea. Rev.*, **134**, 2397–2417, https://doi.org/10.1175/MWR3204.1.

Fu, B., T. Li, M. S. Peng, and F. Weng, 2007: Analysis of tropical cyclogenesis in the western North Pacific for 2000 and 2001. *Wea. Forecasting*, **22**, 763–780, https://doi.org/10.1175/WAF1013.1.

Ge, X., T. Li, and M. S. Peng, 2010: Cyclogenesis simulation of Typhoon Prapiroon (2000) associated with Rossby wave energy dispersion. *Mon. Wea. Rev.*, **138**, 42–54, https://doi.org/10.1175/2009MWR3005.1.

——, ——, and ——, 2013: Tropical cyclone genesis efficiency: Mid-level versus bottom vortex. *J. Trop. Meteor.*, **19**, 197–213.

Gray, W. M., 1968: Global view of the origin of tropical disturbances and storms. *Mon. Wea. Rev.*, **96**, 669–700, https://doi.org/10.1175/1520-0493(1968)096<0669:GVOTOO>2.0.CO;2.

Hendricks, E. A., M. S. Peng, X. Ge, and T. Li, 2011: Performance of a dynamic initialization scheme in the Coupled Ocean–Atmosphere Mesoscale Prediction System for Tropical Cyclones (COAMPS-TC). *Wea. Forecasting*, **26**, 650–663, https://doi.org/10.1175/WAF-D-10-05051.1.

Hirschberg, P. A., and J. M. Fritsch, 1993: On understanding height tendency. *Mon. Wea. Rev.*, **121**, 2646–2661, https://doi.org/10.1175/1520-0493(1993)121<2646:OUHT>2.0.CO;2.

Holland, G. J., 1997: The maximum potential intensity of tropical cyclones. *J. Atmos. Sci.*, **54**, 2519–2541, https://doi.org/10.1175/1520-0469(1997)054<2519:TMPIOT>2.0.CO;2.

Hong, S.-Y., Y. Noh, and J. Dudhia, 2006: A new vertical diffusion package with an explicit treatment of entrainment processes. *Mon. Wea. Rev.*, **134**, 2318–2341, https://doi.org/10.1175/MWR3199.1.

Janjić, Z. I., 1994: The step-mountain eta coordinate model: Further developments of the convection, viscous sublayer, and turbulence closure schemes. *Mon. Wea. Rev.*, **122**, 927–945, https://doi.org/10.1175/1520-0493(1994)122<0927:TSMECM>2.0.CO;2.

——, 2000: Comments on "Development and evaluation of a convection scheme for use in climate models." *J. Atmos. Sci.*, **57**, 3686, https://doi.org/10.1175/1520-0469(2000)057<3686:CODAEO>2.0.CO;2.

Kilroy, G., M. T. Montgomery, and R. K. Smith, 2017a: The role of boundary-layer friction on tropical cyclogenesis and subsequent intensification. *Quart. J. Roy. Meteor. Soc.*, **143**, 2524–2536, https://doi.org/10.1002/qj.3104.

——, R. K. Smith, M. T. Montgomery, 2017b: A unified view of tropical cyclogenesis and intensification. *Quart. J. Roy. Meteor. Soc.*, **143**, 450–462, https://doi.org/10.1002/qj.2934.

Kuo, H.-C., J.-H. Chen, R. T. Williams, and C.-P. Chang, 2001: Rossby waves in zonally opposing mean flow: Behavior in northwest Pacific summer monsoon. *J. Atmos. Sci.*, **58**, 1035–1050, https://doi.org/10.1175/1520-0469(2001)058<1035:RWIZOM>2.0.CO;2.

Lau, K.-H., and N.-C. Lau, 1990: Observed structure and propagation characteristics of tropical summertime synoptic scale disturbances. *Mon. Wea. Rev.*, **118**, 1888–1913, https://doi.org/10.1175/1520-0493(1990)118<1888:OSAPCO>2.0.CO;2.

Li, T., 2006: Origin of the summer time synoptic-scale wave train in the western North Pacific. *J. Atmos. Sci.*, **63**, 1093–1102, https://doi.org/10.1175/JAS3676.1.

——, 2012: Synoptic and climatic aspects of tropical cyclogenesis in Western North Pacific. *Cyclones: Formation, Triggers and Control*, K. Oouchi and H. Fudeyasu, Eds., Nova Science Publishers, 61–94.

——, and B. Fu, 2006: Tropical cyclogenesis associated with Rossby wave energy dispersion of a preexisting typhoon. Part I: Satellite data analyses. *J. Atmos. Sci.*, **63**, 1377–1389, https://doi.org/10.1175/JAS3692.1.

——, ——, X. Ge, B. Wang, and M. Peng, 2003: Satellite data analysis and numerical simulation of tropical cyclone formation. *Geophys. Res. Lett.*, **30**, 2122, https://doi.org/10.1029/2003GL018556.

——, X. Ge, B. Wang, and Y. Zhu, 2006: Tropical cyclogenesis associated with Rossby wave energy dispersion of a preexisting typhoon. Part II: Numerical simulations. *J. Atmos. Sci.*, **63**, 1390–1409, https://doi.org/10.1175/JAS3693.1.

Mlawer, E. J., and Coauthors, 1997: Radiative transfer for inhomogeneous atmospheres: RRTM, a validated correlated-k model for the longwave. *J. Geophys. Res.*, **102**, 16 663–16 682, https://doi.org/10.1029/97JD00237.

Montgomery, M. T., L. L. Lussier III, R. W. Moore, and Z. Wang, 2010: The genesis of Typhoon Nuri as observed during the Tropical Cyclone Structure 2008 (TCS-08) field experiment—Part 1: The role of the easterly wave critical layer. *Atmos. Chem. Phys.*, **10**, 9879–9900, https://doi.org/10.5194/acp-10-9879-2010.

Noh, Y., W.-G. Cheon, S.-Y. Hong, and S. Raasch, 2003: Improvement of the K-profile model for the planetary boundary layer based on large eddy simulation data. *Bound.-Layer Meteor.*, **107**, 401–427, https://doi.org/10.1023/A:1022146015946.

Nolan, D. S., E. D. Rappin, and K. A. Emanuel, 2007: Tropical cyclogenesis sensitivity to environmental parameters in radiative-convective equilibrium. *Quart. J. Roy. Meteor. Soc.*, **133**, 2085–2107, https://doi.org/10.1002/qj.170.

Rajasree, V. P. M., A. P. Kesarkar, J. N. Bhate, V. Singh, U. Umakanth, and T. H. Varma, 2016a: A comparative study on the genesis of north Indian Ocean Tropical Cyclone Madi (2013) and Atlantic Ocean Tropical Cyclone Florence (2006). *J. Geophys. Res. Atmos.*, **121**, 13 826–13 858, https://doi.org/10.1002/2016JD025412.

——, ——, ——, U. Umakanth, V. Singh, and T. Harish Varma, 2016b: Appraisal of recent theories to understand cyclogenesis pathways of Tropical Cyclone Madi (2013). *J. Geophys. Res. Atmos.*, **121**, 8949–8982, https://doi.org/10.1002/2016JD025188.

Reed, R. J., and E. E. Recker, 1971: Structure and properties of synoptic-scale wave disturbances in the equatorial western Pacific. *J. Atmos. Sci.*, **28**, 1117–1133, https://doi.org/10.1175/1520-0469(1971)028<1117:SAPOSS>2.0.CO;2.

Riehl, H., 1948: On the formation of typhoons. *J. Meteor.*, **5**, 247–265, https://doi.org/10.1175/1520-0469(1948)005<0247:OTFOT>2.0.CO;2.

Ritchie, E. A., and G. J. Holland, 1997: Scale interactions during the formation of Typhoon Irving. *Mon. Wea. Rev.*, **125**, 1377–1396, https://doi.org/10.1175/1520-0493(1997)125<1377:SIDTFO>2.0.CO;2.

——, and ——, 1999: Large-scale patterns associated with tropical cyclogenesis in the western Pacific. *Mon. Wea. Rev.*, **127**, 2027–2043, https://doi.org/10.1175/1520-0493(1999)127<2027:LSPAWT>2.0.CO;2.

Schecter, D. A., and D. H. E. Dubin, 1999: Vortex motion driven by a background vorticity gradient. *Phys. Rev. Lett.*, **83**, 2191–2194, https://doi.org/10.1103/PhysRevLett.83.2191.

Skamarock, W. C., and Coauthors, 2008: A description of the Advanced Research WRF version 3. NCAR Tech. Note NCAR/TN-475+STR, 113 pp., https://doi.org/10.5065/D68S4MVH.

Stern, D. P., and F. Zhang, 2013: How does the eye warm? Part I: A potential temperature budget analysis of an idealized tropical cyclone. *J. Atmos. Sci.*, **70**, 73–90, https://doi.org/10.1175/JAS-D-11-0329.1.

Tam, C.-Y., and T. Li, 2006: The origin and dispersion characteristics of the observed tropical summertime synoptic-scale waves over the western Pacific. *Mon. Wea. Rev.*, **134**, 1630–1646, https://doi.org/10.1175/MWR3147.1.

Wang, Z., M. T. Montgomery, and T. J. Dunkerton, 2010a: Genesis of Pre–Hurricane Felix (2007). Part I: The role of the easterly wave critical layer. *J. Atmos. Sci.*, **67**, 1711–1729, https://doi.org/10.1175/2009JAS3420.1.

——, ——, and ——, 2010b: Genesis of Pre–Hurricane Felix (2007). Part II: Warm core formation, precipitation evolution, and predictability. *J. Atmos. Sci.*, **67**, 1730–1744, https://doi.org/10.1175/2010JAS3435.1.

Xu, Y., T. Li, and M. Peng, 2013: Tropical cyclogenesis in the western North Pacific as revealed by the 2008–09 YOTC data. *Wea. Forecasting*, **28**, 1038–1056, https://doi.org/10.1175/WAF-D-12-00104.1.

——, ——, and ——, 2014: Roles of the synoptic-scale wave train, the intraseasonal oscillation, and high-frequency eddies in the genesis of Typhoon Manyi (2001). *J. Atmos. Sci.*, **71**, 3706–3722, https://doi.org/10.1175/JAS-D-13-0406.1.

Yanai, M., T. Maruyama, T. Nitta, and Y. Hayashi, 1968: Power spectra of large-scale disturbances over the tropical Pacific. *J. Meteor. Soc. Japan*, **46**, 308–323, https://doi.org/10.2151/jmsj1965.46.4_308.